How to cite: *Angew. Chem. Int. Ed.* **2021**, *60*, 12074–12081
International Edition: doi.org/10.1002/anie.202101928
German Edition: doi.org/10.1002/ange.202101928

Interfacial Catalysis

Structure Sensitivity of Au-TiO_2 Strong Metal–Support Interactions

Yunshang Zhang[+], Jin-Xun Liu[+], Kun Qian, Aiping Jia, Dan Li, Lei Shi, Jun Hu, Junfa Zhu, and Weixin Huang**

Abstract: *Strong metal–support interactions (SMSI) is an important concept in heterogeneous catalysis. Herein, we demonstrate that the Au-TiO_2 SMSI of Au/TiO_2 catalysts sensitively depends on both Au nanoparticle (NP) sizes and TiO_2 facets. Au NPs of ca. 5 nm are more facile undergo Au-TiO_2 SMSI than those of ca. 2 nm, while TiO_2 {001} and {100} facets are more facile than TiO_2{101} facets. The resulting capsulating TiO_{2-x} overlayers on Au NPs exhibit an average oxidation state between +3 and +4 and a Au-to-TiO_{2-x} charge transfer, which, combined with calculations, determines the Ti:O ratio as ca. 6:11. Both TiO_{2-x} overlayers and TiO_{2-x}-Au interface exhibit easier lattice oxygen activation and higher intrinsic activity in catalyzing low-temperature CO oxidation than the starting Au-TiO_2 interface. These results advance fundamental understanding of SMSI and demonstrate engineering of metal NP size and oxide facet as an effective strategy to tune the SMSI for efficient catalysis.*

Introduction

Metal–support interactions play a key role in modifying the structures and catalytic performance of supported metal catalysts. Firstly postulated in Group 8 and noble metals supported on TiO_2,[1] strong metal–support interactions (SMSI) referring to high-temperature reduction-induced capsulation of supported metal nanoparticles (NPs) by support overlayers,[2] has been recognized as a common phenomenon occurring in reducible oxides-supported Group 8 and noble metals and evolved as one of the most important concepts in heterogeneous catalysis.[3] Recently, the supported metal catalysts exhibiting the SMSI phenomenon have been broadened to oxides and non-oxides supported Au NPs.[4] Several methods[5] different from the traditional high-temperature reduction approach were reported capable of inducing the capsulation of supported metal NPs by support overlayers. Owing to the capsulation of the catalytic active metal NPs, SMSI generally decreases the catalytic activity of supported metal catalysts but can enhance the stability,[4c–e,5c,6] but there are several reports that the capsulating oxide overlayers/metal NPs were more active in catalyzing some specific reactions than the starting metal/oxide catalysts.[5a,7] Despite the long and extensive studies, the origin of SMSI is still debated due to the lack of solid experimental evidence; meanwhile, the structures of capsulating support overlayers and capsulating support overlayers-metal NPs interfaces remain unclear.[2,3,8]

Particle sizes of supported metals[9] and facets of oxide supports[10] are the most important structural factors in oxides-supported metal catalysts, but their effects on the SMSI have been seldom explored. Ultrafine Pt NPs (ca. 1 nm) with a tight particle size distribution[11] and Ni clusters of a very small number of atoms[12] supported on TiO_2 have been recently observed not capsulated upon high-temperature H_2 reduction and Au NPs supported on TiO_2 has been just reported to exhibit size-dependent H_2-reduction temperatures for a full capsulation,[13] indicating the size effect of supported metal NPs for the SMSI. In the present work, employing Au/TiO_2 catalysts with Au NPs of ca. 5 and ca. 2 nm supported on various anatase TiO_2 nanocrystals (NCs) predominantly exposing the {001} (denoted as TiO_2{001}), {100} (denoted as TiO_2{100}) and {101} (denoted as TiO_2{101}) facets, we unambiguously demonstrate that both metal particle size and oxide facet of metal/oxide catalysts exert great influences on the Au-TiO_2 SMSI. Meanwhile, we develop a combined experimental and DFT calculation approach to successfully identify the Ti:O ratio of capsulating TiO_{2-x} overlayer on Au NPs resulting from the Au-TiO_2 SMSI as around 6:11.

[*] Y. Zhang,[+] Prof. J. X. Liu,[+] Prof. K. Qian, Dr. D. Li, Dr. L. Shi, Prof. W. Huang
Hefei National Laboratory for Physical Sciences at the Microscale, University of Science and Technology of China
Hefei 230026 (P. R. China)
E-mail: jxliu86@ustc.edu.cn
huangwx@ustc.edu.cn

Y. Zhang,[+] Prof. J. X. Liu,[+] Prof. K. Qian, A. Jia, Dr. D. Li, Prof. W. Huang
Key Laboratory of Surface and Interface Chemistry and Energy Catalysis of Anhui Higher Education Institutes and Department of Chemical Physics, University of Science and Technology of China
Hefei 230026 (P. R. China)

A. Jia
Key Laboratory of the Ministry of Education for Advanced Catalysis Materials, Institute of Physical Chemistry
Zhejiang Normal University, Jinhua 321004 (China)

Dr. J. Hu, Prof. J. Zhu
National Synchrotron Radiation Laboratory
University of Science and Technology of China
Hefei, Anhui 230029 (China)

Prof. W. Huang
Dalian National Laboratory for Clean Energy
Dalian 116023 (China)

[+] These authors contributed equally to this work.

Supporting information and the ORCID identification number(s) for the author(s) of this article can be found under: https://doi.org/10.1002/anie.202101928.

Results and Discussion

The TiO_2{001}, TiO_2{100}, and TiO_2{101} NCs with similar BET specific surface areas of ca. 100 $m^2 g^{-1}$ (Supporting Information, Table S1) and the proportions of the exposed predominant facets above 80% were prepared following the well-established recipes.[14] It is noteworthy that our as-synthesized TiO_2 NCs do not show XPS signals of F, S, and Cl involved during the synthesis.[14c] TEM and HRTEM images (Figure 1 a–c) show that all TiO_2 NCs exhibit uniform morphologies and a pure anatase phase. Using the TiO_2-fresh NCs as the supports, Au/TiO_2-fresh catalysts with a calculated Au loading of 2% (weight ratio) were prepared by deposition-precipitation method and then treated either by calcination in air at 400 °C for 4 h or by an initial reduction in 5% H_2/Ar at 500 °C for 1 h and subsequent oxidation in 10% O_2/Ar at 400 °C for 1 h. The actual Au loadings of Au/TiO_2-fresh catalysts were analyzed to be close to the calculated loading by inductively coupled plasma atomic emission spectrometry (Supporting Information, Table S2). All Au/TiO_2-fresh catalysts only display diffraction patterns of anatase TiO_2 in the XRD patterns (Supporting Information, Figure S1). Using the TiO_2 {101} diffraction peak, the average crystalline sizes of TiO_2 in various TiO_2 and Au/TiO_2 catalysts were calculated from the Debye–Scherrer equation to improve with the thermal treatments and vary within ca. 10 and ca. 20 nm (Supporting Information, Table S1). HADDF-STEM images demonstrate that the calcination treatment in air leads to supported Au NPs of around 5 nm (Figure 1 d–f; Supporting Information, Figure S2), herein denoted as 5nm-Au/TiO_2-fresh, while the treatment of reduction and subsequent oxidation results in supported Au NPs of around 2 nm (Figure 1 g–i; Supporting Information, Figure S3), herein denoted as 2nm-Au/TiO_2-fresh. The reduction of supported Au^{3+} precursor into Au^0 was observed to occur at higher temperatures upon calcination in air than upon reduction in H_2, resulting in the formation of larger Au NPs.[15] Meanwhile, an O_2 atmosphere was reported to exert a stronger enhancement effect on the Ostwald ripening than a H_2 atmosphere,[16] facilitating the formation of larger supported metal NPs.

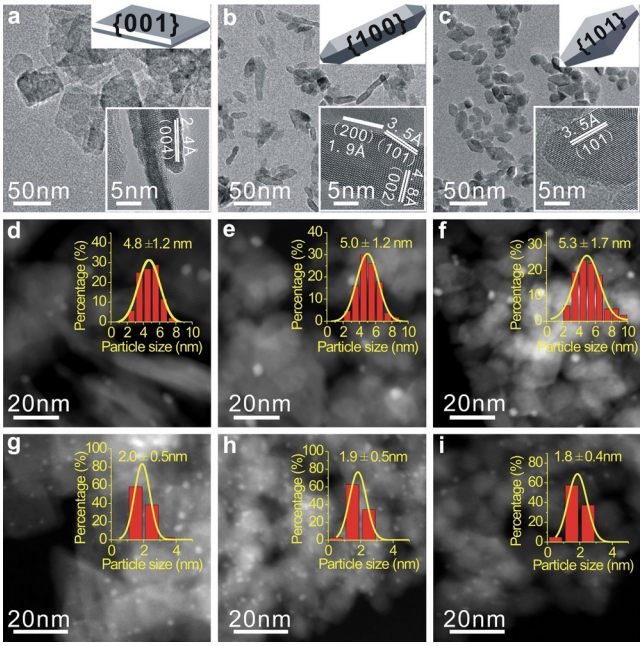

Figure 1. Microscopic characterizations. a)–c) Representative TEM images with inserted HRTEM images and morphology illustrations of a) TiO_2{001}-fresh, b) TiO_2{100}-fresh and c) TiO_2{101}-fresh NCs. d–i) HAADF-STEM images with inserted Au particle size distributions of d) 5nm-Au/TiO_2{001}-fresh, e) 5nm-Au/TiO_2{100}-fresh, f) 5nm-Au/TiO_2{101}-fresh, g) 2nm-Au/TiO_2{001}-fresh, h) 2nm-Au/TiO_2{100}-fresh, and i) 2nm-Au/TiO_2{101}-fresh catalysts.

Surface structures of various Au/TiO_2-fresh catalysts were probed by CO adsorption at 123 K with $P_{CO} = 200$ Pa (Figure 2).Vibrational peaks at ca. 2178, ca. 2127 and ca.

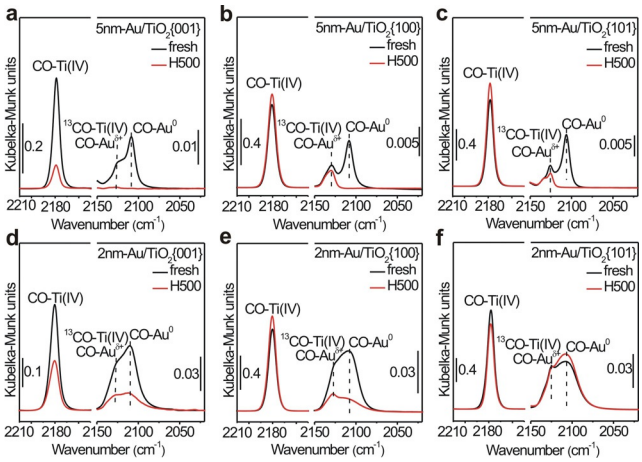

Figure 2. CO adsorption. In situ DRIFTS spectra of CO chemisorption on various Au/TiO_2-fresh and Au/TiO_2-H500 catalysts at 123 K and $P_{CO} = 200$ Pa.

2107 cm^{-1} were observed, arising from CO adsorbed at the Ti^{4+} site ($CO_{Ti^{4+}}$), perimeter $Au^{\delta+}$ site ($CO_{Au^{\delta+}}$) and surface Au^0 site (CO_{Au^0}) of Au NPs, respectively.[17] The strong vibrational peak of $CO_{Ti^{4+}}$ species at ca. 2178 cm^{-1} gives rise to the corresponding weak vibrational peak of $^{13}CO_{Ti^{4+}}$ species at ca. 2127 cm^{-1} (Supporting Information, Figure S4). Due to the higher dispersion of supported Au NPs, the 2nm-Au/TiO_2-fresh catalysts exhibit much stronger vibrational peaks of $CO_{Au^{\delta+}}$ and CO_{Au^0} species than the corresponding 5nm-Au/TiO_2-fresh catalysts. The Au/TiO_2-fresh catalysts were treated in 5% H_2/Ar at 500 °C for 1 h to induce the SMSI. The acquired catalysts, herein denoted as Au/TiO_2-H500, were observed to display Au NP size- and TiO_2 facet-dependent DRIFTS spectra for CO adsorption (Figure 2; Supporting Information, Figures S5 and S6). All 5nm-Au/TiO_2-H500 catalysts exhibit no CO_{Au^0} vibrational feature and a very tiny $CO_{Au^{\delta+}}$ vibrational feature. 2nm-Au/TiO_2{001}-H500 and 2nm-Au/TiO_2{100}-H500 exhibit much weaker vibrational features of both CO_{Au0} and $CO_{Au^{\delta+}}$ species than 2nm-Au/TiO_2{001}-fresh and 2nm-Au/TiO_2{100}-fresh, respectively, and the CO vibrational features on 2nm-Au/TiO_2{001}-H500 are weaker than on 2nm-Au/TiO_2{100}-H500. However, 2nm-Au/TiO_2{101}-H500 shows vibrational features of CO adsorbed at the Au sites almost identical to 2nm-Au/TiO_2{101}-fresh. Meanwhile, the $CO_{Ti^{4+}}$ vibrational

feature weakens upon H_2 reduction at 500 °C for Au/TiO_2{001}-fresh catalysts but does not vary much for Au/TiO_2{100}-fresh and Au/TiO_2{101}-fresh catalysts.

CO adsorption at RT under 1 atm of 1 % CO/Ar was also characterized on various Au/TiO_2-fresh and Au/TiO_2-H500 catalysts (Supporting Information, Figure S7), during which the H_2 reduction treatments in 5 % H_2/Ar at 500 °C were carried out in the in situ reaction cell for DRIFTS. CO does not adsorb at the Ti^{4+} site at RT, and the $CO_{Au^{\delta+}}$ vibrational feature overlaps with the signals of gaseous CO and cannot be observed. Only CO_{Au^0} vibrational features were observed to exhibit results consistent with those of CO adsorption at 123 K. All 5nm-Au/TiO_2-H500 catalysts exhibit no visible CO_{Au^0} vibrational feature, whereas 2nm-Au/TiO_2{001}-H500 and 2nm-Au/TiO_2{100}-H500 exhibit significantly weaker vibrational features than 2nm-Au/TiO_2{001}-fresh and 2nm-Au/TiO_2{100}-fresh, respectively, and 2nm-Au/TiO_2-{101}-H500 shows the vibrational feature almost identical to 2nm-Au/TiO_2{101}-fresh. The CO adsorption behaviors of 5nm-Au/TiO_2-H500 catalysts are the characteristics of SMSI, evidencing the occurrence of Au-TiO_2 SMSI and the consequent almost full capsulation of Au NPs by TiO_{2-x} overlayers. The capacities of Au/TiO_2-H500 catalysts to adsorb CO can fully recover to those of corresponding Au/TiO_2-H500 catalysts after they are oxidized in 10 % O_2/Ar at 400 °C for 1 h (Figure S7), proving the reversibility of Au-TiO_2 SMSI. However, the Au NPs in 2nm-Au/TiO_2{001}-H500 and 2nm-Au/TiO_2{100}-H500 are partially capsulated, and those in 2nm-Au/TiO_2{101}-H500 are barely capsulated.

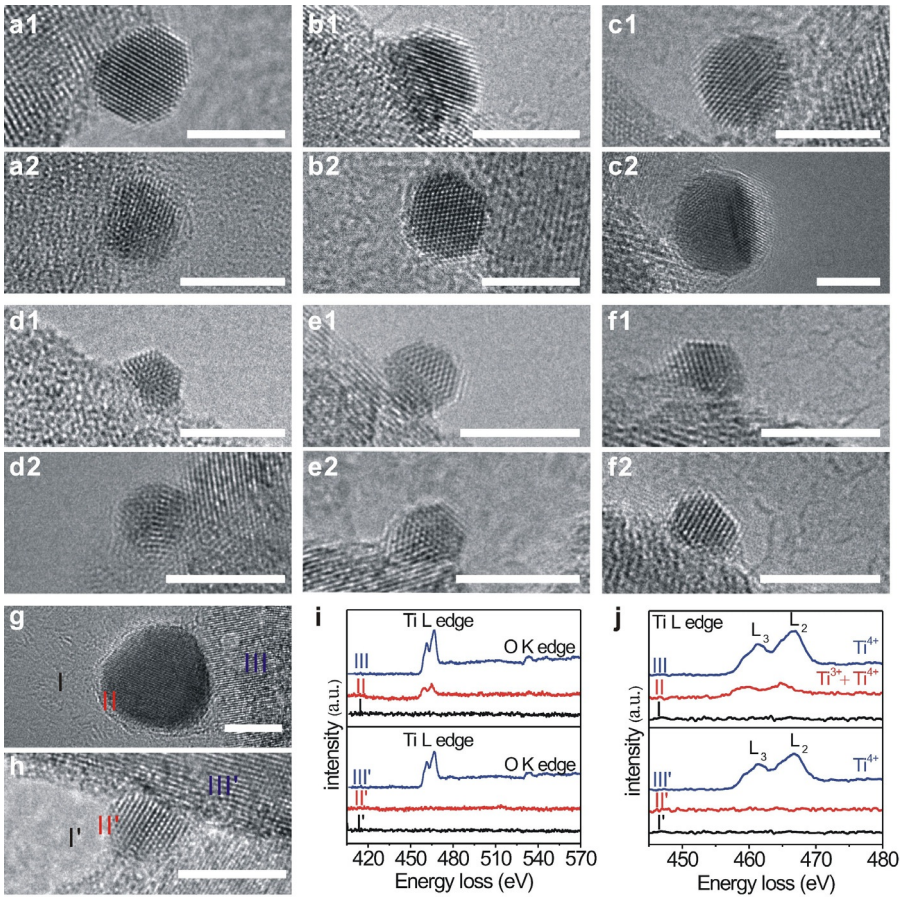

Figure 3. HRTEM images and EELS spectra. a1)–f2) Representative HRTEM images of a1) 5nm-Au/TiO_2{001}-fresh and a2) 5nm-Au/TiO_2{001}-H500, b1) 5nm-Au/TiO_2{100}-fresh and b2) 5nm-Au/TiO_2{100}-H500, c1) 5nm-Au/TiO_2{101}-fresh and c2) 5nm-Au/TiO_2{101}-H500, d1) 2nm-Au/TiO_2-{001}-fresh and d2) 2nm-Au/TiO_2{001}-H500, e1) 2nm-Au/TiO_2{100}-fresh and e2) 2nm-Au/TiO_2-{100}-H500, f1) 2nm-Au/TiO_2{101}-fresh and f2) 2nm-Au/TiO_2{101}-H500. g)–j) HRTEM images and corresponding EELS spectra of marked areas of (g, i and j) 5nm-Au/TiO_2{101}-H500 and (h, i and j) 2nm-Au/TiO_2{101}-H500. The spectra were background-subtracted. The scale bar corresponds to 5 nm.

HRTEM images of various Au/TiO_2-fresh and Au/TiO_2-H500 catalysts (Figure 3a1–f2) directly visualize that the supported Au NPs are obviously capsulated in 5nm-Au/TiO_2-H500 catalysts, partially capsulated in 2nm-Au/TiO_2{001}-H500 and 2nm-Au/TiO_2{100}-H500, and barely capsulated in 2nm-Au/TiO_2{101}-H500. Uniform Ti and O signals were imaged on the Au NPs in the energy-dispersive X-ray (EDX) mapping image of 5nm-Au/TiO_2{101}-H500 (Supporting Information, Figure S8), proving the full capsulation of Au NPs. Electron energy loss spectra (EELS) analysis of marked areas in HRTEM images of 5nm-Au/TiO_2{101}-H500 and 2nm-Au/TiO_2{101}-H500 (Figure 3 g–j; Supporting Information, Figure S9) evidences the presence of both Ti L-edge and O K-edge EELS signals on the surface of Au NP of 5nm-Au/TiO_2{101}-H500 but not on the surface of Au NP of 2nm-Au/TiO_2{101}-H500. This further supports that Au NP of 5nm-Au/TiO_2{101}-H500 are capsulated by TiO_{2-x} overlayers while those of 2nm-Au/TiO_2{101}-H500 are not. Comparing the EELS spectra of TiO_x from TiO to TiO_2,[18] the EELS features of TiO_2 support in 5nm-Au/TiO_2{101}-H500 and 2nm-Au/TiO_2{101}-H500 are the typical features of TiO_2, while the EELS feature of capsulating TiO_{2-x} overlayers on Au NP of 5nm-Au/TiO_2{101}-H500 is similar to that of Ti_5O_9 with mixed valences of Ti^{3+} and Ti^{4+}.

The above spectroscopic and microscopic results clearly demonstrate that the Au-TiO_2 SMSI of Au/TiO_2 catalysts sensitively depends on the Au NP size and the TiO_2 facet. Supported Au NPs with a size of ca. 5 nm are more facile to undergo the Au-TiO_2 SMSI than those of ca. 2 nm, and the TiO_2 {001} and {100} facets are more facile than the TiO_2{101} facets. Such a structure sensitivity of Au-TiO_2 SMSI in Au/TiO_2 catalysts, as far as we know, represents the first unambiguous and comprehensive example of structure sensitivity of SMSI.

The reducibility of various TiO_2-fresh and Au/TiO_2-fresh catalysts was examined using H_2-TPR measurements. TiO_2-{001}-fresh NCs are more difficult to be reduced than TiO_2{100}-fresh and TiO_2{101}-fresh NCs (Supporting Information, Figure S10), consistent with the DFT calculation results of oxygen vacancy formation energies of anatase TiO_2 {001}, {100}, and {101} surfaces as 4.57, 4.0, and 4.15 eV, respectively.[19] The loading of Au NPs induces Au_{NP}-TiO_2 interactions and subsequently promotes the reduction of TiO_2 NCs (Figure 4a–c). The TiO_2 in Au/TiO_2{001}-fresh and Au/

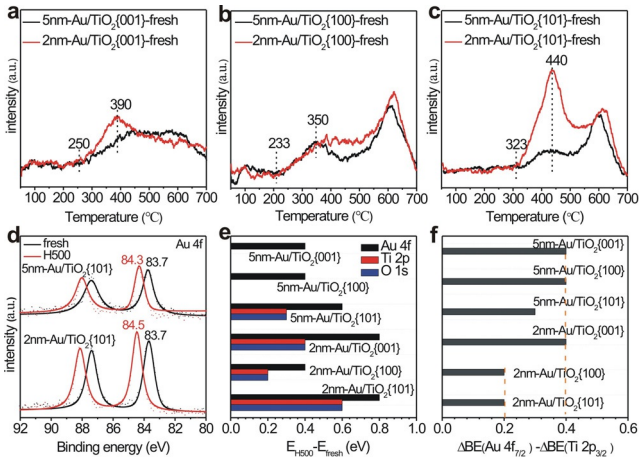

Figure 4. Au-TiO_2 interactions. a)–c) H_2-TPR profiles of a) Au/TiO_2-{001}-fresh, b) Au/TiO_2{100}-fresh and c) Au/TiO_2{101}-fresh. d) Au 4f XP spectra of 5nm-Au/TiO_2{101}-fresh, 5nm-Au/TiO_2{101}-H500, 2nm-Au/TiO_2{101}-fresh and 2nm-Au/TiO_2{101}-H500. e) Au $4f_{7/2}$, Ti $2p_{3/2}$ and O 1s binding energy shifts of Au/TiO_2-fresh catalysts after H500 pretreatments. f) Au $4f_{7/2}$ binding energy shifts of Au/TiO_2-fresh catalysts induced by H500 pretreatments after subtracting the band-bending effects.

TiO_2{100}-fresh is more easily to be reduced than in Au/TiO_2{101}-fresh, which suggests stronger Au_{NP}-TiO_2{001} and Au_{NP}-TiO_2{100} interactions than Au_{NPs}-TiO_2{101} interactions, in line with the results that the TiO_2 {001} and {100} facets are more facile to occur the Au-TiO_2 SMSI than the TiO_2{101} facets. The sizes of supported Au NPs between 2 and 5 nm do not affect the reduction temperature of TiO_2 in Au/TiO_2-fresh catalysts much. 2nm-Au/TiO_2{001}-fresh and 2nm-Au/TiO_2{100}-fresh exhibit slightly enhanced low-temperature reduction peaks than 5nm-Au/TiO_2{001}-fresh and 5nm-Au/TiO_2{100}-fresh, respectively, while 2nm-Au/TiO_2-{101}-fresh exhibits a significantly enhanced low-temperature reduction peak than 5nm-Au/TiO_2{101}-fresh. These observations can be attributed, on one hand, to the longer Au-TiO_2 perimeter of 2nm-Au/TiO_2-fresh than of 5nm-Au/TiO_2-fresh, on the other hand, to the occurrence of Au-TiO_2 SMSI in Au/TiO_2 catalysts except 2nm-Au/TiO_2{101}-fresh during the H_2-TPR process which results in the capsulation of supported Au NPs and subsequent suppression of their promotion effect on TiO_2 reduction.

Various TiO_2 and Au/TiO_2 catalysts before and after H_2 treatment were characterized by XPS without exposure to air. After H_2 reduction at 500 °C, the Ti $2p_{3/2}$ and O 1s binding energies of all TiO_2-H500 NCs were observed to shift toward higher binding energies by the same value of 0.3 eV (Supporting Information, Figure S11 and Table S3). This suggests the occurrence of downward surface band bending with similar extents for all TiO_2-H500 NCs, which, based on the corresponding ESR measurements (Supporting Information, Figure S12), results from the reduction-induced formation of large quantities of bulk F^+ centers. The Au $4f_{7/2}$ binding energy of Au/TiO_2-fresh catalysts locates at 83.5–83.7 eV (Figures 4d; Supporting Information, Figure S13 and Table S4). It shifts toward higher binding energies after H_2 reduction at 500 °C and the amplitudes vary with the catalysts. Based on the Ti 2p and O 1s XPS results (Supporting Information, Figure S14 and Table S4), no surface bend banding occurs for TiO_2 of Au/TiO_2-fresh catalysts, while the downward surface band bending occurs in 5nm-Au/TiO_2{101}-H500 and 2nm-Au/TiO_2-H500 catalysts but not in 5nm-Au/TiO_2{001}- H500 and 5nm-Au/TiO_2{100}-H500 catalysts. The corresponding ESR results (Supporting Information, Figure S15) show the presence of bulk F^+ centers, bulk Ti^{3+} species, and surface O_2^- species in Au/TiO_2-fresh and Au/TiO_2-H500 catalysts, but no Ti^{3+} features could be observed in the Ti 2p XPS and UPS spectra (Supporting Information, Figures S16 and S17). Au/TiO_2{001}-H500, 5nm-Au/TiO_2-{100}-H500 and 5nm-Au/TiO_2{101}-H500 catalysts exhibit much stronger defect signals than corresponding Au/TiO_2-fresh catalysts, while 2nm-Au/TiO_2{100}-H500 and 2nm-Au/TiO_2{101}-H500 catalysts show weaker defect signals than corresponding Au/TiO_2-fresh catalysts. Therefore, the surface band bending of TiO_2 in Au/TiO_2-H500 catalysts seems not dependent on the defect density. We propose that the defects in 5nm-Au/TiO_2{001}-H500 and 5nm-Au/TiO_2{100}-H500 catalysts are so localized not as to induce the downward surface band bending of TiO_2, while those in other Au/TiO_2-H500 catalysts are homogeneously distributed and induce the downward surface band bending of TiO_2.

Figure 4e illustrates the Au $4f_{7/2}$, Ti $2p_{3/2}$, and O 1s binding energy shifts of various Au/TiO_2-H500 catalysts comparing to corresponding Au/TiO_2-fresh catalysts, and Figure 4f shows the Au $4f_{7/2}$ binding energy shifts of various Au/TiO_2-H500 catalysts comparing to corresponding Au/TiO_2-fresh catalysts after the corrections of corresponding surface band bending effects. It can be seen that the H_2 treatment at 500 °C induces the positive shifts in the Au 4f binding energy of supported Au NPs for all Au/TiO_2-fresh catalysts. The charger transfer between supported Au NPs and TiO_2 support is well established.[20] Charge transfer occurs obviously from surface oxygen vacancies of reduced TiO_2 surface to supported Au NPs but is negligible between supported Au NPs and stoichiometric TiO_2 surface. Therefore, the observed positive shifts in the Au 4f binding energy of Au/TiO_2-H500 catalysts should result from the charge transfer from capsulated Au NPs to capsulating TiO_{2-x} overlayers. Similar charge transfer was previously observed from capsulated Pt NPs to capsulating TiO_{2-x} overlayers due to the Pt-TiO_2 SMSI.[21] The Au 4f binding energy shift amplitudes vary with both the size of supported Au NPs and the TiO_2 facets in the same trends to the SMSI effect. Supported on the same type of TiO_2 support, 5 nm Au NPs exhibit larger Au 4f binding energy shifts and more extensive Au-TiO_2 SMSI than 2 nm Au NPs; with

similar sizes, Au NPs supported on TiO_2{001} exhibit larger Au 4f binding energy shifts and more extensive Au-TiO_2 SMSI than on TiO_2{100} and TiO_2{101}. A larger Au 4f binding energy shift points to a more extensive Au_{NP}-to-TiO_{2-x} charge transfer at the TiO_{2-x}-Au_{NP} interface and consequently a stronger TiO_{2-x}-Au_{NP} interactions, triggering a more extensive Au-TiO_2 SMSI.

In the Au-TiO_2 SMSI process, the H_2 reduction at 500 °C induced-transformation of the Au_{NP}-TiO_2 interface of Au/TiO_2-fresh catalysts to the TiO_{2-x}-Au_{NP} interface of Au/TiO_2-H500 catalysts via the removal of the O atom, can be described by the chemical equation of $x\,H_2 + Au_{NP}\text{-}TiO_2 \rightarrow TiO_{2-x}\text{-}Au_{NP} + x\,H_2O$. Thermodynamically, the occurrence of SMSI between supported Au NP and TiO_2 support is favored for Au/TiO_2 catalyst with a strong TiO_{2-x}-Au_{NP} interfacial interactions, a weak Au_{NP}-TiO_2 interfacial interactions, and a weak Ti–O bond. The Ti–O bond strength can be related to the reducibility of TiO_2 in Au/TiO_2 catalysts. As shown in the H_2-TPR profiles, TiO_2 in Au/TiO_2{001}-fresh and Au/TiO_2-{100}-fresh is more easily to be reduced than in Au/TiO_2{101}-fresh, thus the Ti–O bond is weaker in Au/TiO_2{001}-fresh and Au/TiO_2{100}-fresh than in Au/TiO_2{101}-fresh. The strength of both Au_{NP}-TiO_2 and TiO_{2-x}-Au_{NP} interfacial interactions can be related to the interfacial charge transfer. As demonstrated by the Au 4f binding energy, all Au/TiO_2-fresh catalysts exhibit similar Au_{NP} -TiO_2 interfacial interactions, while 5nm-Au/TiO_2-H500 exhibits stronger TiO_{2-x}-Au_{NP} interfacial interactions than corresponding 2nm-Au/TiO_2-H500 and Au/TiO_2{001}-H500 exhibits stronger TiO_{2-x}-Au_{NP} interfacial interactions than corresponding Au/TiO_2-{100}-H500 and Au/TiO_2{101}-H500. Therefore, 5 nm Au NPs supported on TiO_2 are more facile to undergo the Au-TiO_2 SMSI than 2 nm Au NPs, and the TiO_2{001} facet is more facile to undergo the Au-TiO_2 SMSI than the TiO_2{100} facet and then the TiO_2{101} facet. Our observation that 2 nm Au NPs supported on TiO_2{101} do not exhibit the Au-TiO_2 SMSI could be the reason for the absence of Au-TiO_2 SMSI in Au/TiO_2 catalysts since the sizes around 2 nm are very common for Au NPs supported on TiO_2 and the {101} facets are predominant on spherical or irregular anatase TiO_2 particles following the Wulff construction.[22]

The Au particle size-dependent Au_{NP}-to-TiO_{2-x} charge transfer at the TiO_{2-x}-Au_{NP} interface can be associated with the size-dependent electronic structures of Au NPs. Resulted from the interplay of quantum-size and surface effect,[23] the lattice contracts, and the d charge at the metal atom site depletes relative to the bulk metal as the size of metal particles decreases. Supported Au NPs of 2–3 nm were previously reported to exhibit such a metal-to-nonmetal transition.[15,24] Therefore, 2 nm Au NPs with the contracting lattice and the depleted d charge exhibit less extensive Au_{NP}-to-TiO_{2-x} charge transfer at the TiO_{2-x}-Au_{NP} interface than 5 nm Au NPs and consequently are less able to trigger the Au-TiO_2 SMSI. These results provide unambiguous experimental evidence for directly correlating the TiO_{2-x}-Au_{NP} interface formation with the occurrence of Au-TiO_2 SMSI.

Catalytic CO oxidation is very sensitive to structures of employed catalysts.[25] Catalytic activity of various Au/TiO_2-fresh and Au/TiO_2-H500 catalysts was evaluated in low-temperature CO oxidation (Figure 5 a–f; Supporting Information, Figure S18). The 5nm-Au/TiO_2-H500 catalysts with almost fully capsulated Au NPs are less active than the corresponding 5nm-Au/TiO_2-fresh catalysts, whereas the 2nm-Au/TiO_2-H500 catalysts with partially capsulated Au NPs are more active than the corresponding 2nm-Au/TiO_2-fresh catalysts. The best catalyst, 2nm-Au/TiO_2{101}-H500, exhibits a Au mass-specific CO reaction rate as high as 2.75 $mol_{CO}\,g_{Au}{}^{-1}\,h^{-1}$ at 30 °C. All Au/TiO_2-fresh catalysts with the Au_{NP}-TiO_2 interface as the active structure exhibit similar apparent activation energies around 42.2 ± 2.2 kJ mol^{-1}, while all Au/TiO_2-H500 catalysts exhibit similar apparent activation energies of 29.0 ± 2.1 kJ mol^{-1} (Figure 5 g; Supporting Information, Figures S19, S20 and Table S5). Thus, the active structures of all Au/TiO_2-H500 catalysts, which could be the TiO_{2-x}-Au interface or the capsulating TiO_{2-x} overlayers on Au NPs, are intrinsically more active in catalyzing CO oxidation than the Au_{NP}-TiO_2 interface of Au/TiO_2-fresh catalysts. These observations also suggest that, although supported Au NPs on 2nm-Au/TiO_2{101}-fresh are not capsulated upon a H_2 treatment at 500 °C, the interface structure should change from the original Au_{NP}-TiO_2 interface to the capsulating TiO_{2-x}-Au_{NP} interface, resulting from the reduction of TiO_2. The reaction order against CO of Au/TiO_2-H500 catalysts is generally larger than that of corresponding Au/TiO_2-fresh catalysts (Supporting Information, Figures S21, S22 and Table S5), except that 5nm-Au/TiO_2{001}-H500 with a very small amount of surface Au sites exhibits almost identical reaction order against CO to 5nm-Au/TiO_2{001}-fresh. The reaction order against O_2 of Au/TiO_2-H500 catalysts is similar to that of corresponding Au/TiO_2-fresh catalysts.

Using Au/TiO_2{101}-fresh catalysts as an example, CO treatments of 5nm-Au/TiO_2{101}-fresh and 2nm-Au/TiO_2-{101}-fresh at 500 °C also demonstrate the similar Au NP size-dependent Au-TiO_2 SMSI, in which the treated 5 nm- Au/TiO_2{101}-CO500 exhibits the Au-TiO_2 SMSI whereas the treated 2nm-Au/TiO_2{101}-CO500 does not (Supporting Information, Figure S23). Meanwhile, Au/TiO_2{101}-CO500 and Au/TiO_2{101}-H500 show similar catalytic activity and apparent activation energy in catalyzing low-temperature CO

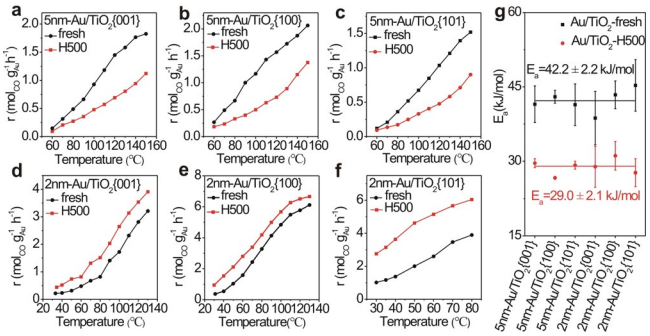

Figure 5. Catalytic performance in CO oxidation. a)–f) Steady-state Au mass-specific CO reaction rate as a function of reaction temperature of CO oxidation catalyzed by Au/TiO_2-fresh and Au/TiO_2-H500 catalysts. Reaction condition: 1 % CO and 0.5 % O_2 balanced with N_2, flow rate: 30 mL min^{-1}. g) Apparent activation energies of low-temperature CO oxidation catalyzed by Au/TiO_2-fresh and Au/TiO_2-H500 catalysts.

oxidation (Supporting Information, Figure S24). These results further confirm the structure sensitivity of Au-TiO_2 SMSI.

DFT calculations were used to probe charge transfer processes between the Au_{NP}-TiO_2 and TiO_{2-x}-Au_{NP} interfaces using two-layer Au rod supported on anatase TiO_2(101) surface and $Ti_{12}O_{24-x}$ clusters ($x=0$–6) on Au(111) as the models (Figure 6), respectively. The two-layer Au nanorod

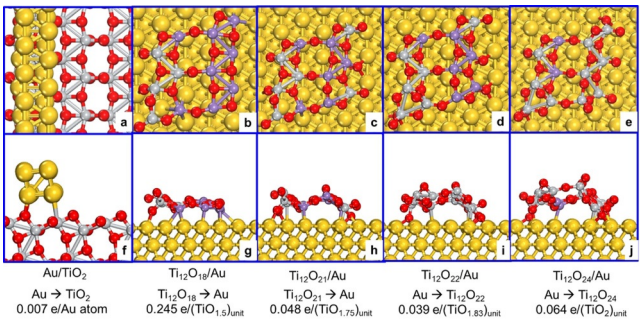

Figure 6. Calculated structures and interfacial charge transfer of Au/TiO_2 and TiO_{2-x}/Au. a)–e) Top and f)–j) side views of optimized Au/TiO_2 and $Ti_{12}O_{24-x}$/Au ($x=0$–6) structures. The Au yellow, Ti^{4+} gray, Ti^{3+} purple, O red spheres. The direction and amount of charge transfer between $Ti_{12}O_{24-x}$ and Au are indicated below the structures.

binds TiO_2(101) surface with the average Au-O and Au-Ti bond lengths, respectively of 2.47 and 3.43 Å, indicating weak Au-TiO_2 interactions. However, large structure reconstructions occurred when one-layer $Ti_{12}O_{24-x}$ ($x=0$–6) structure with the feature of TiO_2(101) surface were deposited on Au(111) surface due to formations of multiple Au−Ti and Au−O bonds. Charge transfer occurs barely at the Au_{NP}-TiO_2 interface, consistent with previous calculation results,[20] but it occurs obviously at the TiO_{2-x}-Au_{NP} interfaces with both direction and amplitude sensitively depending on the TiO_{2-x} composition. As summarized in Table S6, eight Ti^{3+}/four Ti^{4+}, six Ti^{3+}/six Ti^{4+}, six Ti^{3+}/six Ti^{4+}, and two Ti^{3+}/ten Ti^{4+} are in $Ti_{12}O_{18}$, $Ti_{12}O_{21}$, $Ti_{12}O_{22}$, and $Ti_{12}O_{24}$, respectively; meanwhile, one Au−O bond/twelve Au−Ti bonds, five Au−O bonds/ten Au−Ti bonds, nine Au−O bonds/six Au−Ti bonds, and seven Au−O bond and five Au-Ti bonds form at $Ti_{12}O_{18}$/Au(111), $Ti_{12}O_{21}$/Au(111), $Ti_{12}O_{22}$/Au(111), and $Ti_{12}O_{24}$/Au(111) interfaces, respectively. The Bader charge analysis was carried out within the interfacial Au−O and Au−Ti bonds. Charge transfer always occurs from Au to O within the interfacial Au−O bond, and from Ti to Au within the interfacial Au−Ti bond for the Ti cations. Less Au−Ti bonds and more Au−O bonds formation results in the charge transfer direction changing from TiO_x-to-Au to Au-to-TiO_x with increasing O content in $Ti_{12}O_{24-x}$/Au(111) (Figure 6). The overall charge transfer occurs from $Ti_{12}O_{18}$ and $Ti_{12}O_{21}$ clusters to Au(111) with amplitudes of 0.245 *e* per $(TiO_{1.5})_{unit}$ and 0.048 *e* per $(TiO_{1.75})_{unit}$, respectively, whereas from Au(111) to $Ti_{12}O_{22}$ and $Ti_{12}O_{24}$ clusters with amplitudes of 0.039 *e* per $(TiO_{1.83})_{unit}$ and 0.064 *e* per $(TiO_2)_{unit}$, respectively. O/Ti atom ratio was found as a descriptor for the $Ti_{12}O_{24-x}$-Au(111) interfacial charge transfer (Supporting Information, Figure S25).

Experimentally, we observed that the capsulating TiO_{2-x} overlayers on Au NPs exhibit mixed valences of Ti^{3+} and Ti^{4+}, and charge transfer occurs from Au to TiO_{2-x}. Correlated with the calculated Ti^{3+}/Ti^{4+}ions compositions and charge transfers of $Ti_{12}O_{24-x}$/Au(111), it can be identified that the capsulating TiO_{2-x} overlayers on Au NPs in Au/TiO_2 catalysts experiencing Au-TiO_2 SMSI are of a stoichiometric of around $Ti_{12}O_{22}$. Thus, the combined experimental characterizations and DFT calculations of the oxidation state of capsulating oxide overlayers and the metal-capsulating oxide overlayers charge transfer are able to identify the stoichiometric of capsulating oxide overlayers in metal/oxide catalysts experiencing SMSI. This, as far as we know, represents the first approach to identify compositions of capsulating oxide overlayers in metal/oxide catalysts experiencing SMSI.

CO oxidation mechanisms were extensively explored over Au/TiO_2 and $Ti_{12}O_{22}$/Au catalysts. It was found that CO oxidation can occur at the Au-TiO_2 interface of Au/TiO_2(101) surface and the $Ti_{12}O_{22}$-Au interface and on the $Ti_{12}O_{22}$ surface of $Ti_{12}O_{22}$/Au(111) surface, all initiated by the reaction between adsorbed CO and surface lattice O with an activation energy of 0.77, 0.32 and 0.46 eV, respectively (Figure 7; Supporting Information, Figures S26–S31). This produces a CO_2 molecule and an oxygen vacancy at which O_2 adsorbs. After, two CO oxidation pathways were found, depending on whether O_2 dissociates or not.[26] In the direct route, molecularly adsorbed O_2(a) dissociates into one surface lattice oxygen and another atomic oxygen and adsorbed CO reacts with the atomic oxygen to produce a CO_2 molecule, which completes the CO oxidation cycle. In the alternative indirect pathway, adsorbed CO reacts with O_2(a) to form the OCOO intermediate, which subsequently dissociates into a CO_2 molecule and a surface lattice oxygen to complete the CO oxidation cycle. The rate-limiting step in the indirect pathway, the reaction of adsorbed CO reacts with O_2(a) to form the OCOO intermediate, exhibits similar activation energies of around 1.50 eV at the $Ti_{12}O_{22}$-Au interface and on the $Ti_{12}O_{22}$ surface of $Ti_{12}O_{22}$/Au(111) surface, much larger than the rate-limiting step in the direct pathway, the O_2(a) dissociation. Therefore, CO oxidation proceeds via the direct pathway rather than the indirect pathway over $Ti_{12}O_{22}$/Au(111). In contrast, both CO oxidation pathways can take place at the interface of Au/TiO_2, in which CO reacting with lattice oxygen in TiO_2 is the rate-determining step. The O_2(a) dissociation proceeds with similar activation energies at $Ti_{12}O_{22}$-Au interface and on $Ti_{12}O_{22}$ surface of $Ti_{12}O_{22}$/Au-(111), but still lower than that of CO oxidation at the Au-TiO_2 interface of Au/TiO_2(101). Meanwhile, CO oxidation is endothermic at the interface of Au/TiO_2(101) due to the strong Ti−O bond in TiO_2, whereas it becomes highly exothermic thus giving lower CO oxidation barriers at $Ti_{12}O_{22}$-Au interface and on $Ti_{12}O_{22}$ surface of $Ti_{12}O_{22}$/Au-(111). These DFT calculation results demonstrate that $Ti_{12}O_{22}$/Au is more active in catalyzing CO oxidation than Au/TiO_2 catalyst, consistent with the experimental results that all Au/TiO_2-H500 catalysts exhibit lower apparent activation energies in CO oxidation than all Au/TiO_2-fresh catalysts.

Inferred from these DFT calculation results, the likely active structure for catalyzing CO oxidation is the capsulating TiO_{2-x} overlayers in 5nm-Au/TiO_2-H500 catalysts whose Au NPs are almost entirely capsulated, while the capsulating

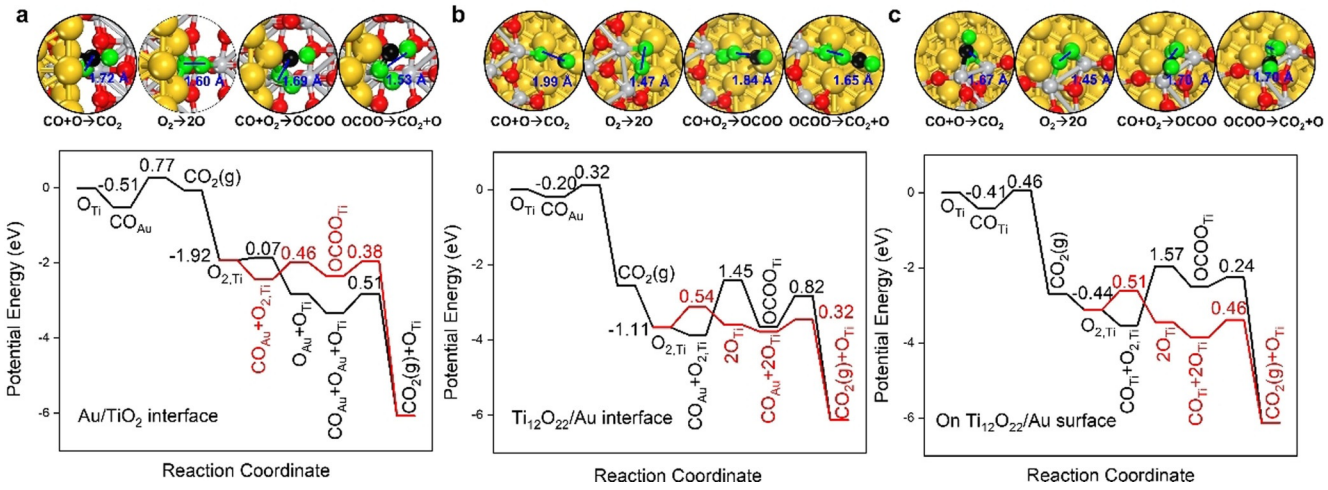

Figure 7. Calculated reaction pathways of CO oxidation. Calculated potential energy diagrams and corresponding key transition states configurations for CO oxidation at the interface of a) Au/TiO_2 and b) $Ti_{12}O_{22}/Au$ and on c) $Ti_{12}O_{22}$ cluster structures. The elementary reaction barriers and the bond distance at the transition state for CO oxidation are indicated in eV and Å, respectively. Au yellow, Ti gray, C black, O red (green) spheres.

TiO_{2-x}-Au interfaces in 2nm-Au/TiO_2-H500 catalysts whose Au NPs are partially capsulated. The experimental results that 2nm-Au/TiO_2-H500 catalysts catalyze CO oxidation more efficiently than 5nm-Au/TiO_2-H500 catalysts suggest that the numbers of active sites created in the capsulating TiO_{2-x}-Au interfaces of 2nm-Au/TiO_2-H500 catalysts are much more than the numbers of active sites created in the capsulating TiO_{2-x} overlayers of 5nm-Au/TiO_2-H500 catalysts. These results point to a strategy to fabricate highly efficient catalysts by manipulating the SMSI effect via engineering metal particle sizes and oxide morphologies of metal/oxide catalysts.

Conclusion

The Au-TiO_2 SMSI of Au/TiO_2 catalysts sensitively depends on both Au NP sizes and TiO_2 facets. Au NPs of ca. 5 nm are more facile undergo the Au-TiO_2 SMSI than those of ca. 2 nm, while TiO_2 {001} and {100} facets are more facile to undergo the Au-TiO_2 SMSI than TiO_2{101} facets. The resulting TiO_{2-x} overlayers on Au NPs exhibit a Ti:O ratio as around 6:11. Both capsulating TiO_{2-x} overlayers on Au NPs and capsulating TiO_{2-x}-Au interface of Au/TiO_2 catalysts experiencing the SMSI exhibit more facile lattice oxygen activation and more intrinsically active in catalyzing low-temperature CO oxidation than the starting Au-TiO_2 interface. These results unambiguously unveil the structure sensitivity of SMSI, which greatly advance fundamental understanding of SMSI and demonstrate engineering of metal NP size and oxide facet as an effective strategy to tune the SMSI for efficient catalysis.

Acknowledgements

This work was financially supported by the National Natural Science Foundation of China (21525313, 91745202, 91945301, 21872128), the Chinese Academy of Sciences, the Changjiang Scholars Program of Ministry of Education of China, University of Science and Technology of China (KY2060000171, KY2060000176).

Conflict of interest

The authors declare no conflict of interest.

Keywords: facet effect · interfacial catalysis · low-temperature CO oxidation · metal–support interactions · size effect

[1] S. J. Tauster, S. C. Fung, R. L. Garten, *J. Am. Chem. Soc.* **1978**, *100*, 170–175.
[2] a) S. Bernal, J. J. Calvino, M. A. Cauqui, J. M. Gatica, C. López Cartes, J. A. Pérez Omil, J. M. Pintado, *Catal. Today* **2003**, *77*, 385–406; b) J. Y. Liu, *ChemCatChem* **2011**, *3*, 934–948.
[3] a) S. J. Tauster, *Acc. Chem. Res.* **1987**, *20*, 389–394; b) G. L. Haller, D. E. Resasco, *Adv. Catal.* **1989**, *36*, 173–235.
[4] a) Y. Kuwauchi, H. Yoshida, T. Akita, M. Haruta, S. Takeda, *Angew. Chem. Int. Ed.* **2012**, *51*, 7729–7733; *Angew. Chem.* **2012**, *124*, 7849–7853; b) X. Y. Liu, M. H. Liu, Y. C. Luo, C. Y. Mou, S. D. Lin, H. K. Cheng, J. M. Chen, J. F. Lee, T. S. Lin, *J. Am. Chem. Soc.* **2012**, *134*, 10251–10258; c) H. Tang, F. Liu, J. Wei, B. Qiao, K. Zhao, Y. Su, C. Jin, L. Li, J. Liu, J. Wang, T. Zhang, *Angew. Chem. Int. Ed.* **2016**, *55*, 10606–10611; *Angew. Chem.* **2016**, *128*, 10764–10769; d) H. Tang, J. Wei, F. Liu, B. Qiao, X. Pan, L. Li, J. Liu, J. Wang, T. Zhang, *J. Am. Chem. Soc.* **2016**, *138*, 56–59; e) H. Tang, Y. Su, B. Zhang, A. F. Lee, M. A. Isaacs, K. Wilson, L. Li, Y. Ren, J. Huang, M. Haruta, B. Qiao, X. Liu, C. Jin, D. Su, J. Wang, T. Zhang, *Sci. Adv.* **2017**, *3*, e1700231; f) J. Dong, Q. Fu, Z. Jiang, B. Mei, X. Bao, *J. Am. Chem. Soc.* **2018**, *140*, 13808–13816.
[5] a) J. C. Matsubu, S. Zhang, L. DeRita, N. S. Marinkovic, J. G. Chen, G. W. Graham, X. Pan, P. Christopher, *Nat. Chem.* **2017**, *9*, 120–127; b) J. Zhang, H. Wang, L. Wang, S. Ali, C. Wang, L. Wang, X. Meng, B. Li, D. S. Su, F. S. Xiao, *J. Am. Chem. Soc.* **2019**, *141*, 2975–2983; c) S. Liu, W. Xu, Y. Niu, B. Zhang, L. Zheng, W. Liu, L. Li, J. Wang, *Nat. Commun.* **2019**, *10*, 5790.

[6] T. W. van Deelen, C. Hernández Mejía, K. P. de Jong, *Nat. Catal.* **2019**, *2*, 955 – 970.
[7] a) L. Fan, K. Fujimoto, *J. Catal.* **1994**, *150*, 217 – 220; b) Y. Zhang, X. Yang, X. Yang, H. Duan, H. Qi, Y. Su, B. Liang, H. Tao, B. Liu, D. Chen, X. Su, Y. Huang, T. Zhang, *Nat. Commun.* **2020**, *11*, 3185.
[8] a) S. J. Tauster, S. C. Fung, *J. Catal.* **1978**, *55*, 29 – 35; b) M. S. Spencer, *J. Catal.* **1985**, *93*, 216 – 223; c) Y. Gao, Y. Liang, S. A. Chambers, *Surf. Sci.* **1996**, *365*, 638 – 648; d) S. Labich, E. Taglauer, H. Knözinger, *Top. Catal.* **2000**, *14*, 153 – 161; e) Q. Fu, T. Wagner, S. Olliges, H. D. Carstanjen, *J. Phys. Chem. B* **2005**, *109*, 944 – 951; f) Q. Fu, T. Wagner, *Surf. Sci. Rep.* **2007**, *62*, 431 – 498; g) M. G. Willinger, W. Zhang, O. Bondarchuk, S. Shaikhutdinov, H. J. Freund, R. Schlögl, *Angew. Chem. Int. Ed.* **2014**, *53*, 5998 – 6001; *Angew. Chem.* **2014**, *126*, 6108 – 6112.
[9] a) J. H. Sinfelt, *Catal. Rev.* **1970**, *3*, 175 – 205; b) M. Haruta, *Catal. Today* **1997**, *36*, 153 – 166; c) L. Liu, A. Corma, *Chem. Rev.* **2018**, *118*, 4981 – 5079.
[10] a) W. Huang, *Acc. Chem. Res.* **2016**, *49*, 520 – 527; b) S. Chen, F. Xiong, W. Huang, *Surf. Sci. Rep.* **2019**, *74*, 100471.
[11] M. Macino, A. J. Barnes, S. M. Althahban, R. Qu, E. K. Gibson, D. J. Morgan, S. J. Freakley, N. Dimitratos, C. J. Kiely, X. Gao, A. M. Beale, D. Bethell, Q. He, M. Sankar, G. J. Hutchings, *Nat. Catal.* **2019**, *2*, 873 – 881.
[12] X. Zhang, P. Yan, B. Zhao, K. Liu, M. C. Kung, H. H. Kung, S. Chen, Z. C. Zhang, *ACS Catal.* **2019**, *9*, 3551 – 3563.
[13] X. Du, Y. Huang, X. Pan, B. Han, Y. Su, Q. Jiang, M. Li, H. Tang, G. Li, B. Qiao, *Nat. Commun.* **2020**, *11*, 5811.
[14] a) X. Han, Q. Kuang, M. Jin, Z. Xie, L. Zheng, *J. Am. Chem. Soc.* **2009**, *131*, 3152 – 3153; b) L. Liu, X. Gu, Z. Ji, W. Zou, C. Tang, F. Gao, L. Dong, *J. Phys. Chem. C* **2013**, *117*, 18578 – 18587; c) D. Li, R. You, M. Yang, Y. Liu, K. Qian, S. Chen, T. Cao, Z. Zhang, J. Tian, W. Huang, *J. Phys. Chem. C* **2019**, *123*, 10367 – 10376.
[15] K. Qian, L. Luo, H. Bao, Q. Hua, Z. Jiang, W. Huang, *Catal. Sci. Technol.* **2013**, *3*, 679 – 687.
[16] N. Masoud, T. Partsch, K. P. de Jong, P. E. de Jongh, *Gold Bull.* **2019**, *52*, 105 – 114.
[17] D. Li, S. Chen, R. You, Y. Liu, M. Yang, T. Cao, K. Qian, Z. Zhang, J. Tian, W. Huang, *J. Catal.* **2018**, *368*, 163 – 171.
[18] E. Stoyanov, F. Langenhorst, G. Steinle-Neumann, *Am. Mineral.* **2007**, *92*, 577 – 586.
[19] H. Cheng, A. Selloni, *Phys. Rev. B* **2009**, *79*, 092101.
[20] a) R. Meyer, C. Lemire, S. K. Shaikhutdinov, H. J. Freund, *Gold Bull.* **2004**, *37*, 72 – 124; b) K. Okazaki, Y. Morikawa, S. Tanaka, K. Tanaka, M. Kohyama, *Phys. Rev. B* **2004**, *69*, 235404; c) Z. Jiang, W. Zhang, L. Jin, X. Yang, F. Xu, J. Zhu, W. Huang, *J. Phys. Chem. C* **2007**, *111*, 12434 – 12439.
[21] Z. Wu, Y. Li, W. Huang, *J. Phys. Chem. Lett.* **2020**, *11*, 4603 – 4607.
[22] a) M. Lazzeri, A. Vittadini, A. Selloni, *Phys. Rev. B* **2001**, *63*, 155409; b) G. Liu, H. G. Yang, J. Pan, Y. Q. Yang, G. Q. Lu, H. M. Cheng, *Chem. Rev.* **2014**, *114*, 9559 – 9612.
[23] M. Bäumer, H. J. Freund, *Prog. Surf. Sci.* **1999**, *61*, 127 – 198.
[24] M. Valden, X. Lai, D. W. Goodman, *Science* **1998**, *281*, 1647 – 1650.
[25] a) N. Li, Q. Y. Chen, L. F. Luo, W. X. Huang, M. F. Luo, G. S. Hu, J. Q. Lu, *Appl. Catal. B* **2013**, *142*, 523 – 532; b) Y. Zhou, D. E. Doronkin, M. Chen, S. Wei, J.-D. Grunwaldt, *ACS Catal.* **2016**, *6*, 7799 – 7809; c) Y.-G. Wang, D. C. Cantu, M.-S. Lee, J. Li, V.-A. Glezakou, R. Rousseau, *J. Am. Chem. Soc.* **2016**, *138*, 10467 – 10476.
[26] J. X. Liu, Y. Su, I. A. W. Filot, E. J. M. Hensen, *J. Am. Chem. Soc.* **2018**, *140*, 4580 – 4587.

Manuscript received: February 7, 2021
Revised manuscript received: March 7, 2021
Accepted manuscript online: March 11, 2021
Version of record online: April 16, 2021

